Available online at www.sciencedirect.com

SCIENCE @ DIRECT®

International Journal of Heat and Mass Transfer 47 (2004) 4205–4213

International Journal of HEAT and MASS TRANSFER

www.elsevier.com/locate/ijhmt

Navier–Stokes simulation of the flow field in laterally driven microcomb structures

Ching-Shung Chen *

Department of Aerospace Engineering, Tamkang University, Tamsui, Taiwan 251, China

Received 24 July 2003; received in revised form 6 May 2004
Available online 2 July 2004

Abstract

The Navier–Stokes equations were used to simulate two laterally driven microcomb structures in this study. The total quality factors predicted numerically agree quite well with the experimental data. The numerical results show that the bottom surface of the oscillating structure contributes about 66% of the total damping and is very close to that predicted by the Couette flow model. The top, side, and edge surface each contributes about 10–12%. The flow above the oscillating structure is far from the Stokes flow due to the curvilinear fluid motion generated by the pumping and sucking motions of the oscillating structure. Lifting the gap between the oscillating structure and the substrate is an effective way to reduce the total damping, and its effectiveness was investigated. The magnitude of the amplitude of the oscillating structure was found to have very minor effect on the damping. The slip effect was also included in this study. The slip effect reduces the viscous damping on the bottom surface of the oscillating structure by about 7%.

© 2004 Elsevier Ltd. All rights reserved.

Keywords: Microcomb structure; Viscous damping; Squeeze damping

1. Introduction

The high strength and stable mechanical properties of silicon together with the on going advances in semiconductor fabrication techniques make it possible to make high performance microsensors with high resolution, accuracy, repeatability, and low cost. Among these new devices are laterally driven microactuators and microsensors. In contrast to vertically driven devices, with damping provided by a fluid squeeze-film produced by the relative axial or tilting motion of two closely spaced plates [1], the viscous shear in the thin fluid film is the dominant damping mechanism in laterally driven microstructures.

Cho et al. [2] demonstrated the attractive features of laterally driven microstructures by resonant sensors and actuators, frequency selective microfilters, and damped microaccelerometers. The damping level of a microstructure plays an important role in the performance of a system. For example, small damping leads to a high quality factor, Q. The quality factor is defined as the total energy stored in a microstructure divided by the sum of energy losses from the vibrating elements. Stemme [3] showed that a high Q simplifies the feedback control of the control loop and gives better resolution and stability. Cho et al. [2] also showed that adequate damping is needed to obtain flat output signals over wide frequency ranges and prevent amplitude and phase distortions.

Among the factors that affect the dynamic performance of a resonant sensor, such as mass, resonant frequency, stiffness, and damping, damping is the most difficult to estimate. This is because there are several damping mechanisms related to the total Q, for example, viscous and acoustic dampings, damping due to imbalance in the structure, and damping resulting from internal material related losses [3]. Viscous damping due to the interaction between the vibrating structure and the surrounding fluid (mostly air) is the dominant damping mechanism in most resonant sensors. Yet, it is

---

* Tel.: +886-2-26215656x2577; fax: +886-2-26209746.
E-mail address: cschen@mail.tku.edu.tw (C.-S. Chen).

0017-9310/$ - see front matter © 2004 Elsevier Ltd. All rights reserved.
doi:10.1016/j.ijheatmasstransfer.2004.05.007

Nomenclature

d	distance between the oscillating structure and the substrate, m
D	dissipation energy, J
E	strain energy of the comb structure, J
h	height of the oscillating structure, m
K	equivalent stiffness of the supporting tethers for the seismic mass, N/m
Kn	Knudsen number $(=\frac{\lambda}{d})$
L	length of the oscillating structure, m
M	mass of the movable comb structure, kg
p	dimensional pressure, Pa
$\bar{p}$	nondimensional pressure $(=(p-p_\infty)/(\mu U_0/d))$
p_∞	atmospheric pressure, Pa
Q	quality factor $(=2\pi\frac{E}{D})$
Re	Reynolds number $(=\frac{\rho U_0 d}{\mu})$
St	Strouhal number $(=\frac{d\omega}{U_0})$
u	dimensional velocity in the x-direction, m/s
$\bar{u}$	nondimensional velocity in the $\bar{x}$-direction
U_0	lateral velocity of the oscillating structure, m/s
v	dimensional velocity in the y-direction, m/s
$\bar{v}$	nondimensional velocity in the $\bar{y}$-direction
x	dimensional x-coordinate, m
$\bar{x}$	nondimensional x-coordinate
y	dimensional y-coordinate, m
$\bar{y}$	nondimensional y-coordinate
Greek symbols	
λ	mean free path of air molecules, m
ν	kinetic viscosity, m^2/s
ω	resonant frequency of the oscillating structure, rad/s
ρ	air density, kg/m^3
σ	ratio of diffusively reflected molecules
τ	nondimensional time $(=\omega t)$

the most difficult to estimate accurately, because the flow is highly nonlinear. Fig. 1 shows a typical laterally driven microcomb structure, consisting of a mass suspended with tethers anchored onto the sensor body. The lateral motion of the vibrating structure alters the area of the capacitor and changes the output voltage. To maintain system sensitivity, the stiffness of the supporting tethers should be kept small.

The dynamic performance of laterally driven microcomb structures was studied experimentally as well as analytically by several investigators. Tang et al. [4,5] investigated viscous air damping in microcomb structures based on a Couette flow model. The theoretically estimated Q-factors, although qualitatively consistent with the measured Q, were much higher than the measured values. Cho et al. [2,6] studied this problem using a Stokes flow model. The Q-factors calculated using the Stokes flow model were in better agreement with the experimental data than that computed using the Couette flow model. However, large discrepancies still remained between the analytical and measured Q values. Zhang and Tang [7] developed an empirical formula based on experimental data to include the edge and finite-size effects. This formula was based on a very limited database and has not been validated extensively. Ye et al. [8] investigated this problem using a boundary element method. The numerically predicted Q-factor is within 10% of the experimental data, but only one set of data was compared. The details of the flow field cannot be shown by the boundary element method. The slip effect was also not included in the investigation.

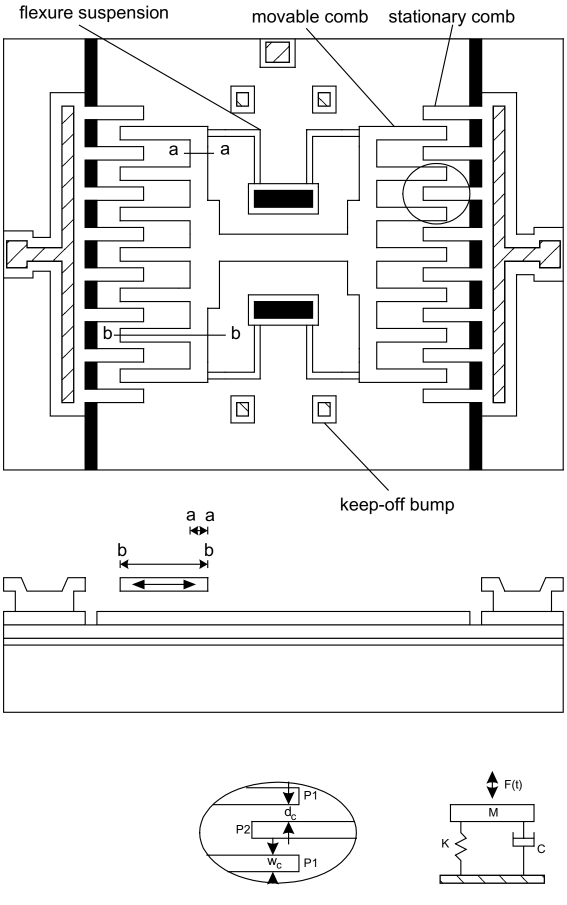

Fig. 1. The schematic diagram of a microcomb structure.

The Couette and Stokes flow models assume that the vibrating structure is infinite; while in reality it is finite. The effects of the pumping and sucking motions generated by the edges of the vibrating structure are unknown. The purpose of this study is to develop a numerical scheme that is able to simulate the flow field around a comb structure, so that the edge and finite-size effects can be understood. The Knudsen number in typical microcomb structures indicates that part of the flow is in the slip flow region. The slip effect is also included in this study.

2. Analytical solutions

2.1. The flow solution in region I

To simplify the solution procedure, we assumed that the flow in a cut-off plane (a–a or b–b in Fig. 1) parallel to the oscillating direction of the comb structure is two-dimensional. In deriving the analytical solutions (Fig. 2), the oscillating structure was assumed to be infinite, the flow in region I becomes a flow over an impulsively started oscillating plate. The $\bar{v}$ velocity vanishes. The governing equation and the corresponding boundary conditions are

$$\gamma \frac{\partial \bar{u}}{\partial \tau} = \frac{\partial^2 \bar{u}}{\partial \bar{y}^2} \tag{1}$$

$$\bar{u} = \cos\tau \quad \text{for } \bar{y} = \frac{d+h}{d}$$
(on the top surface of the oscillating structure) (2)

$$\bar{u} = 0 \quad \text{for } \bar{y} \to \infty$$
(far away from the oscillating structure) (3)

In the above equations $\bar{u}$, $\bar{v}$ are the nondimensional velocities in the $\bar{x}$- and $\bar{y}$-direction, respectively. The physical quantities are normalized using the following relations

$$\bar{x} = x/d, \quad \bar{y} = y/d, \quad \bar{u} = u/U_0, \quad \bar{v} = v/U_0, \quad \tau = \omega t$$

The parameter γ is defined as $\gamma = St \cdot Re$, Re and St are the Reynolds number and Strouhal number, respectively, and are defined by $Re = \rho U_0 d/\mu$, $St = d\omega/U_0$. The parameters U_0 and ω are the velocity and resonant frequency of the oscillating structure, respectively. The parameter d is the gap between the oscillating structure and the substrate and μ is the absolute viscosity of air.

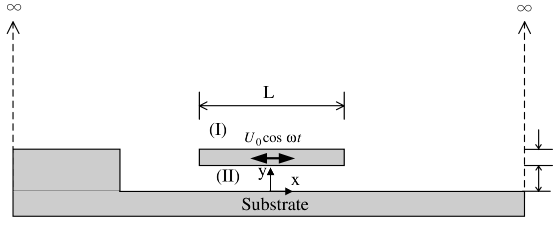

Fig. 2. The coordinate system for the analytical and numerical solutions.

The problem described above is the so-called Stokes' second problem [9]. Eq. (1) is a parabolic equation that can be solved using the separation of variables method [10]. The result is

$$\begin{aligned}\bar{u}(\tau,\bar{y}) = -\frac{2}{\sqrt{\pi}} \int_0^{\frac{1}{2}\sqrt{\frac{\gamma}{\tau}}\left(\bar{y}-\frac{d+h}{d}\right)} &\cos\left(\tau - \frac{\gamma}{4\xi^2}\left(\bar{y} - \frac{d+h}{d}\right)\right) \\ &\cdot \exp(-\xi^2)\,\mathrm{d}\xi + \exp\left(-\sqrt{\frac{\gamma}{2}}\left(\bar{y} - \frac{d+h}{d}\right)\right) \\ &\cdot \cos\left(\tau - \sqrt{\frac{\gamma}{2}}\left(\bar{y} - \frac{d+h}{d}\right)\right)\end{aligned} \tag{4}$$

The first term in the above equation represents the transient motion, which dies down after some time. The second term denotes the steady state motion. The energy dissipated by the viscous shear on the top surface per oscillating cycle can be calculated using

$$D_{\text{top}} = \int_{A_{\text{top}}} \int_0^{2\pi/\omega} \chi_{\text{w}} \cdot U_0 \cos\omega t \cdot \mathrm{d}t \cdot \mathrm{d}A \tag{5}$$

The parameter χ_{w} is the viscous shear at the wall and $U_0 \cos\omega t$ is the velocity of the oscillating structure.

2.2. The flow solution in region II

The governing equation and the corresponding boundary conditions for the flow in region II (Fig. 2) are

$$\gamma \frac{\partial \bar{u}}{\partial \tau} = \frac{\partial^2 \bar{u}}{\partial \bar{y}^2} \tag{6}$$

$$\bar{u} = 0 \quad \text{for } \bar{y} = 0 \qquad \text{(on the silicon substrate)} \tag{7}$$

$$\bar{u} = \cos\tau \quad \text{for } \bar{y} = 1$$
(on the bottom surface of the oscillating structure) (8)

Eq. (6) is a parabolic equation that can be solved using the separation of variables method [11,12]. The result is

$$\begin{aligned}\bar{u}(\tau,\bar{y}) = 2\sum_{n=1}^{\infty} \frac{(-1)^n \beta_n^3}{\beta_n^4 + \gamma^2} \sin(\beta_n \bar{y}) \exp(-\beta_n^2 \tau/\gamma) \\ + \bar{y}\cos\tau + 2\sum_{n=1}^{\infty} \frac{(-1)^n \beta_n \gamma}{\beta_n^4 + \gamma^2} \\ \times \sin(\beta_n \bar{y}) \left(\frac{\gamma}{\beta_n^2}\cos\tau + \sin\tau\right)\end{aligned} \tag{9}$$

where $\beta_n = n\pi$. The first term in the above equation represents the transient motion, which dies down after some time. The second and third terms denote the steady state motion. The energy dissipated by the viscous shear on the bottom surface per oscillating cycle can be calculated using Eq. (5).

The strain energy of a microcomb structure is

$$E = \frac{1}{2\omega} U_0^2 \sqrt{MK} \tag{10}$$

where M is the seismic mass of the microcomb structure and K denotes the equivalent stiffness of the supporting tethers for the seismic mass. The strain energy of a microcomb structure is dissipated by the viscous shear on the top, bottom, and side surfaces plus the squeezing drag on the edge surfaces of the oscillating structure. The quality factor, Q, is defined as

$$Q = 2\pi \frac{E}{D} \tag{11}$$

where $D = D_{\text{top}} + D_{\text{bottom}} + D_{\text{side}} + D_{\text{edge}}$. The damping ratio of a microcomb structure is defined by $\varsigma = \frac{1}{2Q}$. The damping on the side surfaces of the oscillating comb fingers can be calculated in a way similar to that on the bottom surface, because the flow in the side regions is similar to that in region II (Figs. 1 and 2).

3. Numerical solutions

3.1. The numerical boundary conditions

The nondimensional boundary conditions are

(1) $\bar{u} = \bar{v} = 0$, on the surfaces of fixed structures.
(2) $\bar{u} = \cos\tau$, $\bar{v} = 0$, on the surfaces of the oscillating structure.
(3) $\frac{\partial \bar{u}}{\partial \bar{y}} = \frac{\partial \bar{v}}{\partial \bar{y}} = 0$, $\bar{p} = 0$, as $\bar{y} \to \infty$.
(4) $\frac{\partial \bar{u}}{\partial \bar{x}} = \frac{\partial \bar{v}}{\partial \bar{x}} = \frac{\partial \bar{p}}{\partial \bar{x}} = 0$, on the right and left boundaries.
(5) the slip boundary conditions were used if the slip flow was assumed.

The mean free path λ of the air under standard atmospheric conditions is about 0.06 μm. The gap d between the oscillating structure and the substrate for a typical microcomb structure is about 2 μm (region II of Fig. 2). The Knudsen number in region II is $Kn = \lambda/d = 0.03$, which indicates that the flow is in the slip flow region and the slip effect must be taken into account. For slip flows, the fluid can be assumed to be a continuum but the slip boundary condition must be utilized to account for the incomplete momentum exchange between the gas molecules and the walls. The slip boundary condition on the bottom surface (region II of Fig. 2) of the oscillating structure is [13]

$$\bar{u}_{\text{w}} = -\frac{2-\sigma}{\sigma} Kn \left(\frac{\partial \bar{u}}{\partial \bar{y}} \right)_{\text{w}} + \cos\tau \tag{12}$$

The parameter σ is the ratio of diffusively reflected molecules from the wall. The slip boundary condition on the substrate surface is [13]

$$\bar{u}_{\text{w}} = \frac{2-\sigma}{\sigma} Kn \left(\frac{\partial \bar{u}}{\partial \bar{y}} \right)_{\text{w}} \tag{13}$$

In general, σ may depend on the surface' roughness, temperature, and the gas type. Historically, $\sigma = 1$ has been used for almost all engineering applications [14], although values of σ less than one have been reported under controlled test conditions [15]. Measurements or direct computation of accommodation coefficients for microdevices are very difficult to obtain. The only available accommodation coefficients for microchannel flows were obtained by Arkilic [16]. The working fluids were nitrogen, argon, and carbon dioxide. The microchannel was made from prime silicon crystal. The measured σ is about 0.8. Lower σ is possible due to the low surface roughness of prime silicon crystal. We assumed that $\sigma = 1$ in this study. The slip boundary conditions were applied in region II within the left and right edges of the oscillating structure (Fig. 2).

3.2. The numerical procedure

To simulate the motion of the oscillating structure, the computations were conducted on the transformed coordinate system (ξ, η), where $\bar{x} = \bar{x}(\xi)$, $\bar{y} = \bar{y}(\eta)$. The transformed governing equations are

$$\frac{1}{\bar{x}_\xi} \frac{\partial \bar{u}}{\partial \xi} + \frac{1}{\bar{y}_\eta} \frac{\partial \bar{v}}{\partial \eta} = 0 \tag{14}$$

$$St \cdot Re \frac{\partial \bar{u}}{\partial \tau} + Re \left(\bar{u} \frac{1}{\bar{x}_\xi} \frac{\partial \bar{u}}{\partial \xi} + \bar{v} \frac{1}{\bar{y}_\eta} \frac{\partial \bar{u}}{\partial \eta} \right) = -\frac{1}{\bar{x}_\xi} \frac{\partial \bar{p}}{\partial \xi} + \left[\frac{1}{\bar{x}_\xi} \frac{\partial}{\partial \xi} \left(\frac{1}{\bar{x}_\xi} \frac{\partial \bar{u}}{\partial \xi} \right) + \frac{1}{\bar{y}_\eta} \frac{\partial}{\partial \eta} \left(\frac{1}{\bar{y}_\eta} \frac{\partial \bar{u}}{\partial \eta} \right) \right] \tag{15}$$

$$St \cdot Re \frac{\partial \bar{v}}{\partial \tau} + Re \left(\bar{u} \frac{1}{\bar{x}_\xi} \frac{\partial \bar{v}}{\partial \xi} + \bar{v} \frac{1}{\bar{y}_\eta} \frac{\partial \bar{v}}{\partial \eta} \right) = -\frac{1}{\bar{y}_\eta} \frac{\partial \bar{p}}{\partial \eta} + \left[\frac{1}{\bar{x}_\xi} \frac{\partial}{\partial \xi} \left(\frac{\partial \bar{v}}{\partial \xi} \right) + \frac{1}{\bar{y}_\eta} \frac{\partial}{\partial \eta} \left(\frac{1}{\bar{y}_\eta} \frac{\partial \bar{v}}{\partial \eta} \right) \right] \tag{16}$$

To avoid pressure oscillations, the Marker and Cell (MAC) finite difference scheme in conjunction with a stagger grid was utilized [17]. A typical grid is shown in Fig. 3. The gap d in region II was used as the characteristic length. The mesh in the $\bar{x}$-direction was regenerated after each time step to comply with the movement of the oscillating structure. The velocities and pressure were interpolated from the old mesh into the new mesh accordingly. The mesh in the $\bar{y}$-direction was unchanged during the simulation because the structure did not move in that direction. An explicit finite difference

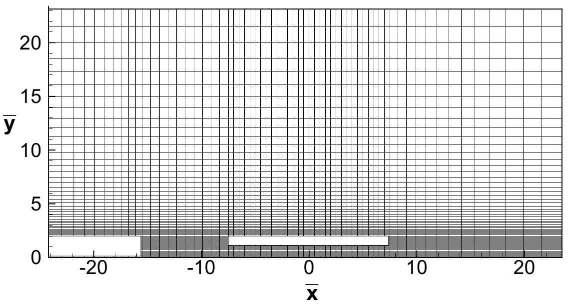

Fig. 3. A typical grid mesh for the numerical simulations.

scheme was used to discretize the governing equations. The convection and diffusion terms in the governing equations were central differenced. The nonlinear terms in the finite difference equations were linearized by lagging the coefficients.

The momentum equations, Eqs. (15) and (16), were differentiated with respect to $\bar{x}$ and $\bar{y}$, respectively, and added together to obtain a Poisson equation for pressure.

$$\frac{\partial^2 \bar{p}}{\partial \bar{x}^2} + \frac{\partial^2 \bar{p}}{\partial \bar{y}^2} = -St \cdot Re \frac{\partial \bar{S}}{\partial \tau} - Re \frac{\partial^2 \bar{u}^2}{\partial \bar{x}^2} - 2Re \frac{\partial (\bar{u}\bar{v})}{\partial \bar{x} \partial \bar{y}} - Re \frac{\partial^2 \bar{v}}{\partial \bar{y}^2} + \frac{\partial^2 \bar{S}}{\partial \bar{x}^2} + \frac{\partial^2 \bar{S}}{\partial \bar{y}^2} \tag{17}$$

where $\bar{S} = \frac{\partial \bar{u}}{\partial \bar{x}} + \frac{\partial \bar{v}}{\partial \bar{y}}$. The expression $\bar{S}^{n+1} = (\frac{\partial \bar{u}}{\partial \bar{x}} + \frac{\partial \bar{v}}{\partial \bar{y}})^{n+1}$ in the $\frac{\partial \bar{S}}{\partial \tau}$ term was set equal to zero, because when the pressure field converges at the $n + 1$ time step the continuity equation should be satisfied [17].

In the numerical simulations, the Poisson equation, Eq. (17), was solved first by iteration to obtain the pressure. The convergence criterion for the pressure field was $\sum |\bar{p}^{k+1}_{i,j} - \bar{p}^{k}_{i,j}| \leqslant 10^{-4}$, the superscription k is the iteration number. After convergence, the pressure was then substituted into the momentum equations, Eqs. (15) and (16), to solve for the $\bar{u}$ and $\bar{v}$ velocities. This completed one time step. This process continued until the periodic steady state was reached. The convergence criterion for the periodic steady state was $\sum |\bar{u}^{n+1}_{i,j} - \bar{u}^{n}_{i,j}| \leqslant 10^{-4}$, where n is the oscillating cycles of the structure. This criterion was applied at the beginning of each new oscillating cycle to check for convergence. If the criterion was met then the calculation stopped. This process was time accurate. The computer program was first validated by simulating the Stokes' second problem [9]. The oscillating frequency of the infinite plate was assumed to be $\omega = 8$ kHz. The numerically calculated shear stress was compared with the analytical shear stress calculated using Eq. (4) at several different time intervals. The difference was less than 1%. The numerically calculated velocity profile along the $\bar{y}$-axis at several time intervals was also compared with that calculated using Eq. (4). The difference was less than 0.6%.

Table 1
Dimensions and parametric values for the first microcomb structure [2]

Structure thickness	h	1.8 μm
Gap between the oscillating structure and the substrate	d	2.0 μm
Finger width	w_c	4.0 μm
Gap between the oscillating and fixed fingers	d_c	2.0 μm
Effective damping area on the top or bottom surface of the oscillating structure		2.930×10^4 μm^2
Effective damping area on the side surfaces of the oscillating comb fingers		0.540×10^4 μm^2
Effective area on the edges of the oscillating structure		0.147×10^4 μm^2
Equivalent stiffness	K	3.08×10^{-7} N/μm
Effective mass	M	0.123 μg
Resonant frequency	ω	7.98 kHz
Oscillating amplitude		$3d$, $5d$, $7d$
Length of the oscillating structure		$15d$
Reynolds number, Re		1.333×10^{-2}
Strouhal number, St		1.002

A grid independence test was carried out to ensure that the numerical results do not depend on the grid size. A 59×45 grid, a 65×52 grid, and a 75×62 grid were simulated for the case listed in Table 1. Their corresponding total Q values were 15.98, 15.41, and 15.49. The 65×52 grid was chosen for all the simulations in this study. The stability constraint was dominated by the parameter $Re \cdot St$. For the first microcomb structure configuration described in Table 1, a very small time step, $\Delta\tau = 4.189 \times 10^{-5}$, was required in the numerical simulations due to its small $Re \cdot St$ value. It took about 2 h CPU time in a Pentium IV 2.0G PC to run an oscillating cycle. Three oscillating cycles were required to reach the periodic steady state.

4. Results and discussions

After validation using the Stokes second problem, the numerical procedure was then used to calculate the flow field of the first microcomb structure. The dimensions and required parameters of this model are listed in Table 1 [2]. The amplitude of the oscillating electrode was set to $7d$ so that the motion of the electrode can be seen more clearly. Fig. 4 shows the partially magnified velocity vector-plots at $\tau = \pi, \frac{5\pi}{4}, \frac{3\pi}{2}, \frac{7\pi}{4}, 2\pi$ after the periodic steady state was reached. The boundary conditions were the slip conditions. At $\tau = \pi$, Fig. 4(a), the

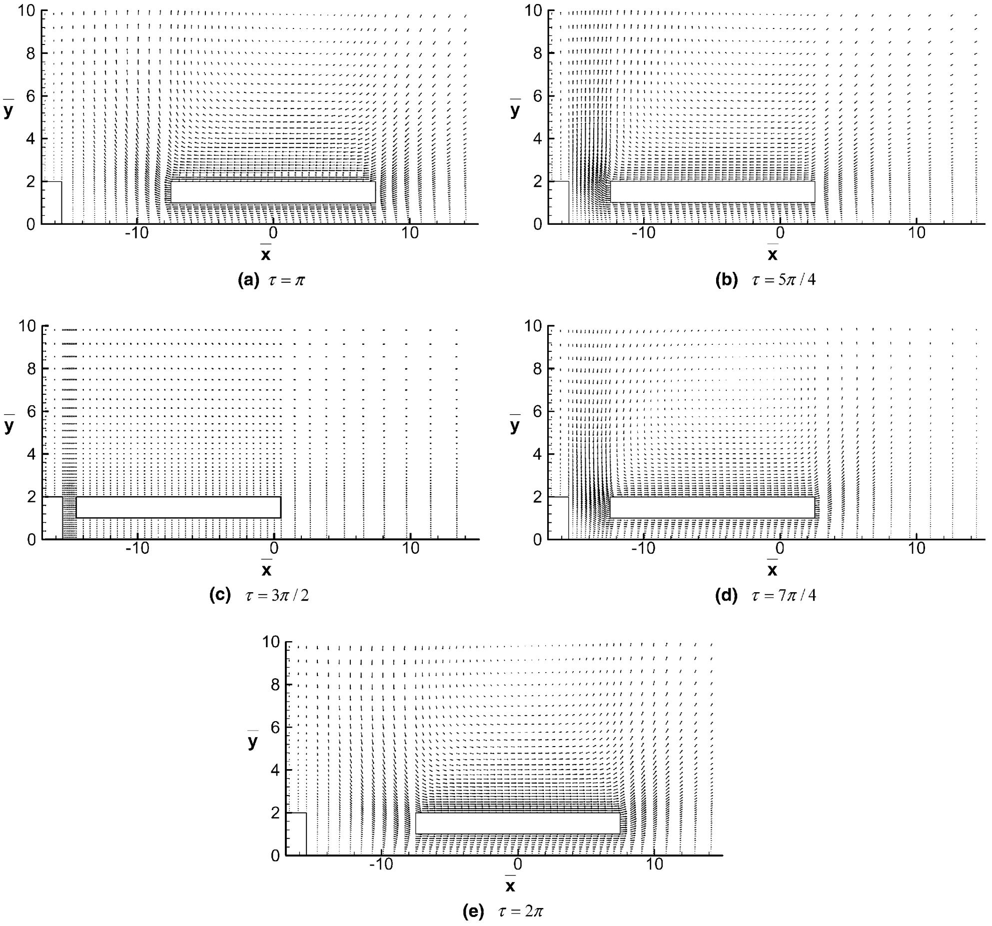

(a) $\tau = \pi$

(b) $\tau = 5\pi/4$

(c) $\tau = 3\pi/2$

(d) $\tau = 7\pi/4$

(e) $\tau = 2\pi$

Fig. 4. Velocity vector-plots of the first microcomb structure at $\tau = \pi, 5\pi/4, 3\pi/2, 7\pi/4, 2\pi$ after the periodic steady state was reached.

oscillating structure is moving to the left at its maximum negative velocity, $-U_0$. The flow field is not symmetrical, because there is a solid block on the left-bottom corner. At $\tau = \frac{5\pi}{4}$, Fig. 4(b), the flow pattern is similar to that at $\tau = \pi$, but the velocity is smaller since the oscillating structure is moving at a smaller velocity. The flow is nearly quiescent at $\tau = \frac{3\pi}{2}$, Fig. 4(c). The velocity of the oscillating structure is zero at this instant. The flows at $\tau = \frac{7\pi}{4}$ and $\tau = 2\pi$, Fig. 4(d) and (e), are similar to that at $\tau = \frac{5\pi}{4}$ and $\tau = 2\pi$ but with opposite directions. As demonstrated in Fig. 4(a), the flow in region II resembles the Couette flow (a linear velocity profile between two parallel plates). The flow in region I is quite different from the Stokes flow. For the Stokes flow the velocity vectors are straight, but the numerical velocity vectors in region I of Fig. 4 are curvilinear due to the pumping and sucking motions of the edge surfaces of the oscillating structure. The curvilinear fluid motion in region I slows down the fluid velocity in the $\bar{x}$-direction and increases the viscous damping on the top surface of the oscillating structure.

Damping affects amplitude as well as frequency in a microcomb structure. Damping is therefore an important design parameter. The quality factor of a microcomb structure is defined by $\frac{1}{Q_{\text{total}}} = \frac{1}{Q_{\text{bottom}}} + \frac{1}{Q_{\text{top}}} + \frac{1}{Q_{\text{side}}} + \frac{1}{Q_{\text{edge}}}$. To calculate Q numerically, the oscillating structure length, L (Fig. 2), was assumed constant. The width of the oscillating structure was the effective top (or bottom) damping area divided by the length. The energy dissipated due to the pressure drag on the edge surfaces of the oscillating structure was calculated using

$$D_{\text{edge}} = \int_{A_{\text{sidI}}} \int_0^{2\pi/\omega} \Delta p \cdot U_0 \cos \omega t \cdot \mathrm{d}t \cdot \mathrm{d}A \tag{18}$$

where Δp is the pressure difference between the right and left edge surfaces of the oscillating structure.

Table 3 compares the analytical, numerical, and experimental Q-factors for the first microcomb structure, Table 1. The oscillation amplitude of the moving electrode was $3d$. As demonstrated in Table 3, the numerical simulations subject to the slip boundary conditions show that the contributions to the total damping by the bottom, top, and side surfaces of the oscillating structure are 65.83%, 11.79%, and 12.42%, respectively. The damping on the edge surfaces contributes another 9.94%. The damping on the bottom, top, and side surfaces is due to viscous stress. The damping on the edge surfaces is the result of pressure difference on the right and left surfaces of the oscillating structure, which is induced by the pumping and sucking motions of the moving structure. The bottom surface is the major damping contributor due to the small gap in region II. The top, side, and edge surfaces have approximately equal contribution to the total damping, around 10–12%.

Although the area of the edge surfaces is only 5% of the top surface, the damping of the former is only 16% less than that of the latter. The *Q*-factors on the side surfaces in Table 3 were all calculated using Eqs. (5) and (9) because we did not simulate the flow on the side regions numerically. The numerical *Q*-factor on the bottom surface of the oscillating structure is very close to the analytical *Q*-factor. This shows that the flow in region II can be modeled by the Couette flow quite well. The velocity vector-plots in Fig. 4 also support this conclusion. The numerical *Q*-factor on the top surface is lower than the analytical *Q*-factor by about 53%. This means that the numerically predicted damping is higher than the analytical damping by about 114%. The reason was explained in the second paragraph of this section. The slip boundary conditions in region II increase the damping on the bottom surface of the oscillating structure by about 7% but have negligible effect on the damping of the top, side, and edge surfaces.

The total *Q*-factor calculated numerically subject to the slip boundary conditions agrees well with the experimental *Q*-factor. The difference is about 7%. Fig. 5 compares the numerical, analytical, and experimental *Q*-factors [2]. The test [2] was repeated ten times. The analytical *Q*-factor did not include the pressure damping on the edge surfaces. This is also the way the *Q*-factors were calculated by some previous investigators [2,4–6]. The results of this study show that the pressure damping on the edge surfaces, slip effect, and the increased damping due to the curvilinear fluid motion in region I are the major sources of error between the analytical and experimental *Q*-factors. Their corresponding percentage errors are about 8.5%, 3.5%, and 8.5%, respectively.

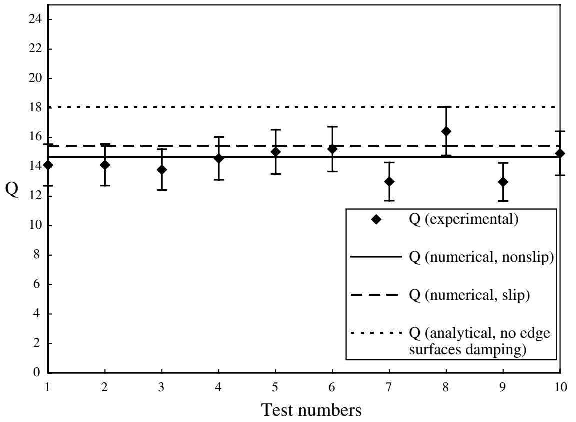

Fig. 5. Comparison of the analytical, numerical, and experimental *Q*-factors [2] for the first model microcomb structure.

Table 2
Dimensions and parametric values for the second microcomb structure [8]

Structure thickness	h	1.96 μm
Gap between the oscillating structure and the substrate	d	2.0 μm
Finger width	w_c	2.0 μm
Gap between the oscillating and fixed fingers	d_c	2.88 μm
Effective damping area on the top or bottom surface of the oscillating structure		1.151×10^4 μm^2
Effective damping area on the side surfaces of the oscillating comb fingers		0.220×10^4 μm^2
Effective area on the edges surfaces of the oscillating structure		0.0695×10^4 μm^2
Equivalent stiffness	K	5.11×10^{-7} N/μm
Effective mass	M	0.035 μg
Resonant frequency	ω	19.2 kHz
Oscillating amplitude		$3d$
Length of the oscillating structure		$15d$
Reynolds number, *Re*		1.333×10^{-2}
Strouhal number, *St*		2.413

Table 4 compares the numerical, analytical, and experimental *Q*-factors for the second microcomb structure. The dimensions and parameters of the second microcomb structure are listed in Table 2. For the slip boundary conditions, the bottom, top, side, and edge surfaces contribute 65.86%, 14.07%, 8.89%, and 11.38% to the total damping, respectively. The slip conditions in region II reduces the damping on the bottom surface of the oscillating structure by about 7% and have negligible effect on the damping of the other surfaces. The total *Q*-factor calculated numerically subject to the slip conditions agrees very well with the experimental *Q*-factor. Table 4 also lists the numerical results obtained by Ye et al. [8] using a boundary element method. The boundary conditions were nonslip. The results of Ye et al. show that the bottom surface contributes 55% of the total damping, which is less than our prediction of 66%. The top surface contributes 12% of the total damping, which is close to our prediction. The side and edge surfaces contribute another 33%. They did not separate the contributions of side and edge surfaces. Their predicted total Q-factor is 25.16, which is close to our nonslip prediction of 25.53. Our results show that the damping on the bottom surface can be predicted quite well by the Couette-flow model (a linear velocity profile between two parallel plates), but Ye et al. predict a smaller damping, the reason is unclear.

Results in Tables 3 and 4 reveal that the viscous damping on the bottom surface contributes about 65% to the total damping. It is logical that we investigate the effect of varying the gap d in region II on the flow field. Table 5 compares the Q on different surfaces subject to different gaps, $d = 2$, 4, 6 μm, for the first microcomb structure. The boundary conditions were slip conditions. Increasing d from 2 to 4 and 6 μm decreases the damping on the bottom surface by about 44% and 59%, respectively. It also reduces the pressure drag on the edge surfaces by 25% and 33%, respectively. But it has very minor effect on the damping of the top surface.

It is also interesting to study the effect of different oscillation amplitudes of the electrode on the flow field. We simulated three different amplitudes ($= 3d$, $5d$, $7d$) for the first microcomb structure. All the other dimensions and parameters are the same as those listed in Table 1. The boundary conditions were slip conditions. For the amplitude $= 7d$ case, the distance between the fixed and oscillating electrodes was only 1 μm when the moving electrode arrived at its left most position. Table 6 lists the numerical Q-factors for the three different amplitude cases. As demonstrated in Table 6, changing amplitude from $3d$ to $5d$ has essentially no effect on the damping. Increasing amplitude from $3d$ to $7d$ has no effect on the damping of the bottom surface, but increases the pressure damping on the edge surfaces and the viscous damping on the top surface by 13% and 4%, respectively. This is because when the distance between the fixed and the moving electrodes becomes very small, the squeezing and therefore the pressure drag increases. The stronger squeezing forces more fluid to move up-

Table 3
Comparison of the analytical, numerical, and experimental Q-factors on the different surfaces of the first microcomb structure

	Top surface	Bottom surface	Side surfaces	Edge surfaces	Total
Numerical Q-factors subject to the nonslip boundary conditions	130.67	21.72	124.06	154.89	14.66
Numerical Q-factors subject to the slip boundary conditions	130.75	23.41	124.06	155.04	15.41
Analytical Q-factors, nonslip boundary conditions	279.64	22.86	124.06		18.06
Experimental Q-factor					14.42

Table 4
Comparison of the analytical, numerical, and experimental Q-factors on the different surfaces of the second microcomb structure

	Top surface	Bottom surface	Side surfaces	Edge surfaces	Total
Numerical Q-factors subject to the nonslip boundary conditions	190.60	37.93	301.77	235.57	25.53
Numerical Q-factors subject to the slip boundary conditions	190.70	40.85	301.77	235.83	26.83
Numerical results obtained by Ye et al. [8]	209.67	45.75	76.24		25.16
Analytical Q-factors, nonslip boundary conditions	315.33	39.99	301.77		31.76
Experimental Q-factor					27

Table 5
Comparison of the numerical (slip boundary conditions) Q-factor on different surfaces of the first microcomb structure subject to three different gaps between the oscillating structure and the substrate

	Top surface	Bottom surface	Side surfaces	Edge surfaces	Total
Numerical Q-factor subject to gap $= 1d$	130.75	23.41	124.06	155.04	15.41
Numerical Q-factor subject to gap $= 2d$	138.63	41.99	124.06	206.30	22.76
Numerical Q-factor subject to gap $= 3d$	142.38	56.47	124.06	232.52	26.96

Table 6
Comparison of the numerical (slip boundary conditions) Q-factor on different surfaces of the first microcomb structure subject to three different oscillating amplitudes of the electrode

	Top surface	Bottom surface	Side surfaces	Edge surfaces	Total
Numerical Q-factors subject to amplitude $= 3d$	130.75	23.41	124.06	155.04	15.41
Numerical Q-factors subject to amplitude $= 5d$	130.60	23.38	124.06	150.75	15.36
Numerical Q-factors subject to amplitude $= 7d$	136.44	23.24	124.06	137.54	15.22

ward, the streamlines in region I become more curvilinear and the viscous drag increases correspondingly. The effect of changing amplitude on damping is much less than what we have thought originally.

5. Conclusions

Numerical results of this study show that the viscous drag on the bottom surface of the oscillating structure is the major contributor of the total damping. It makes up 66% of the total damping for the two microcomb structures investigated. The flow in region II can be modeled and predicted quite well by the Couette flow model. The slip boundary conditions reduce the viscous damping on the bottom surface by about 7%, but have negligible effect on the damping of the other surfaces as were demonstrated in Tables 3 and 4. The top, side, and edge surfaces each contributes about 10–12% of the total damping. Although the area of the edge surfaces is only 5% of the top surface, it contributes about the same amount of damping as that of the top surface. The flow above the top surface, region I, cannot be modeled by the Stokes flow. Instead of the straight streamlines predicted by the Stokes flow model, the pumping and sucking motions of the edge surfaces generate curvilinear streamlines, which increases the viscous drag on the top surface. The total Q-factor predicted numerically subject to the slip boundary conditions agree very well with the experimental data for the two microcomb structures simulated in this study. Increasing the gap between the oscillating structure and the substrate is an effective way to reduce the damping of a microcomb structure as was shown in Table 5. Changing the amplitude of the oscillating electrode has only minor effect on the damping of a microcomb structure as was demonstrated in Table 6.

References

[1] T. Veijola, H. Kuisma, J. Lahdenpera, T. Ryhanen, Equivalent-circuit model of the squeezed gas film in a silicon accelerometer, Sensors Actuators A 48 (1995) 239–248.

[2] Y.H. Cho, B.M. Kwak, A.P. Pisano, R.T. Howe, Viscous energy dissipation in laterally oscillating planar microstructures: a theoretical and experimental study, in: Proceedings of the IEEE Workshop on Microelectromechanical Systems, 1993, pp. 93–98.

[3] G. Stemme, Resonant silicon sensors, J. Micromech. Microeng. 1 (1991) 113–125.

[4] W.C. Tang, T.C. Nguyen, R.T. Howe, Laterally driven polysilicon resonant microstructures, Sensors Actuators A 20 (1989) 25–32.

[5] W.C. Tang, T.C. Nguyen, M.W. Judy, R.T. Howe, Electrostatic-comb drive of lateral polysilicon resonators, Sensors Actuators A 21–23 (1990) 328–331.

[6] Y.H. Cho, A.P. Pisano, R.T. Howe, Viscous damping model for laterally oscillating microstructures, J. Microelectromech. Syst. 3 (2) (1994) 81–87.

[7] X. Zhang, W.C. Tang, Viscous air damping in laterally driven microresonators, in: Proceedings of the IEEE Workshop on Microelectromechanical Systems, 1994, pp. 199–204.

[8] W. Ye, X. Wang, W. Hemmert, D. Freeman, J. White, Viscous drag on a lateral micro-resonator: fast 3-D fluid simulation and measured data, in: Solid-State Sensor and Actuator Workshop, Hilton Head, South Carolina, 2000, pp. 124–127.

[9] I.G. Currie, Fundamental Mechanics of Fluids, second ed., McGraw Hill, New York, 1993, pp. 224–232.

[10] H.S. Carslaw, J.C. Jaeger, Conduction of Heat in Solids, second ed., Clarendon Press, Sydney, 1959, pp. 58–73.

[11] V.S. Arpaci, Conduction Heat Transfer, Addison-Wesley, Massachusetts, 1966, pp. 307–314.

[12] M.N. Ozisik, Heat Conduction, Wiley, New York, 1980, pp. 200–205.

[13] C.S. Chen, C.F. Chou, Analytical and numerical studies on viscous energy dissipation in laterally driven microcomb structures, Int. J. Heat Mass Transfer 46 (4) (2003) 695–704.

[14] E.B. Arkilic, M.A. Schmidt, Gaseous slip flow in long microchannels, J. Microelectromech. Syst. 6 (2) (1997) 167–178.

[15] G.E. Karniadakis, A. Beskok, Micro Flows—Fundamentals and Simulation, Springer-Verlag, Berlin, 2002, pp. 45–53.

[16] E. Arkilic, Measurement of the mass flow and tangential momentum accommodation coefficient in silicon micromachined channels, PhD thesis, Massachusetts Institute of Technology, Boston, MA, 1997.

[17] K.A. Hoffman, S.T. Chiang, Computational Fluid Dynamics for Engineers: Volume I, Engineering Education System, Wichita, Kansas, 1993, pp. 288–343.